# Studies of Pulsed-DC Plasma Actuator and Its effect on Turbulent Boundary Layers Using Novel Optical Diagnostics

John Sontag[1], Stanislav Gordeyev[2], Alan Doung[3], Flint O. Thomas[4] and Thomas C. Corke[5]
*University of Notre Dame, Notre Dame, IN, 46556*

**Non-intrusive optical approach was used to provide additional information about the changes in the turbulent boundary layer, caused by pulsed-DC plasma actuator. Measurements of the plasma actuator in still air revealed that the actuator introduces velocity perturbations in the order of one m/sec. Temporally-spatially-resolved wavefronts were collected in the spanwise direction inside the boundary layer immediately above the plasma actuator. The data were used to extract the convective velocity profiles in the wall-normal direction, as well as to extract deflection angle spectra at various wall-normal locations. While the plasma actuator in previous studies was demonstrated to provide significant reduction in the skin friction, both the velocity profiles and the deflection angle spectra were found to be mostly unaffected by the plasma actuator. These results were found to be consistent with the velocity measured downstream of the actuator.**

## I.    Introduction

Recently reported [1,2] turbulent boundary layer drag reduction experiments performed at the University of Notre Dame have demonstrated unprecedented levels of drag reduction in excess of 70%. These experiments have utilized flush mounted arrays of multiple pulsed-DC plasma actuators that provide a spanwise flow confined to the viscous sublayer. The control flow is designed to intervene in the autonomous near-wall cycle of turbulence generation described by Schoppa and Hussain [3]. Those authors describe a streak transient growth (STG) mechanism in which x-dependent spanwise velocity disturbances lead to an order-of magnitude amplification culminating in the formation of streamwise vortices via nonlinear processes.  It is apparent that drag can be reduced by weakening the turbulent boundary layer streamwise vortices. It then follows that if STG can be prevented, so too will streamwise vortex formation. A key parameter affecting STG is the wall normal vorticity, $\omega_y$, flanking low-speed steaks. If this can be reduced through the prevention of low speed streak lift up, the STG will be prevented. The pulsed-DC plasma actuators produce a spanwise mean flow that prevents the lift-up of low speed streaks, thereby limiting the wall normal vorticity, $\omega_y$. The degree of drag reduction has been shown to depend on both the applied voltage which sets the plasma induced control flow speed and the spanwise inter-electrode spacing which control the number of low-speed streaks that are simultaneously controlled. Figure 1 presents representative results for a turbulent boundary layer. The ordinate presents the percent change in drag as a function of viscous wall units between

---

[1] Graduate student, Department of Aerospace and Mech. Eng  AIAA Student member.
[2] Associate Professor, Department of Aerospace and Mech. Eng., AIAA Associate Fellow
[3] Graduate student, Department of Aerospace and Mech. Eng, AIAA Student member.
[4] Professor, Aerospace and Mechanical Engineering, University of Notre Dame, AIAA Associate Fellow
[5] Professor, Aerospace and Mechanical Engineering, University of Notre Dame, AIAA Fellow.

adjacent surface electrode pairs. The actuators were operated at 6 kV DC and both tripped and untriped boundary layer cases are shown. Peak drag reduction of 70% occurs for an electrode spacing of 800-1000 viscous wall units which corresponds to the simultaneous control of 8-10 low speed streaks. In addition, over most of the cycle the input power for pulsed-DC, $P_{in} = V\,I$, is extremely small. The low required input power for the pulsed-DC actuator poses a large advantage in drag reduction applications where net power savings are required.
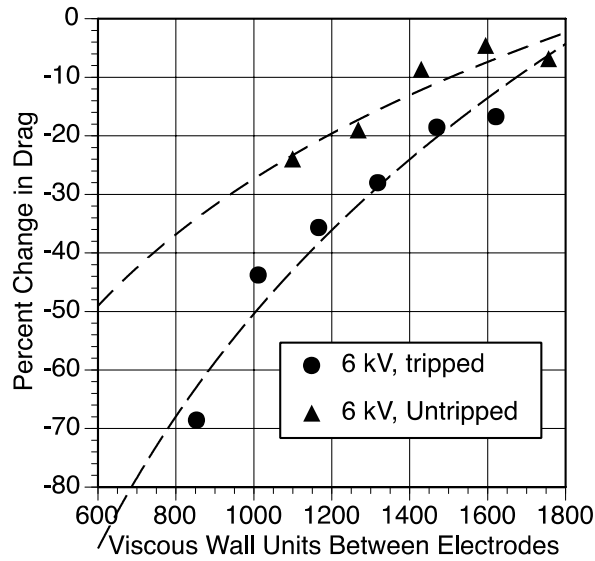


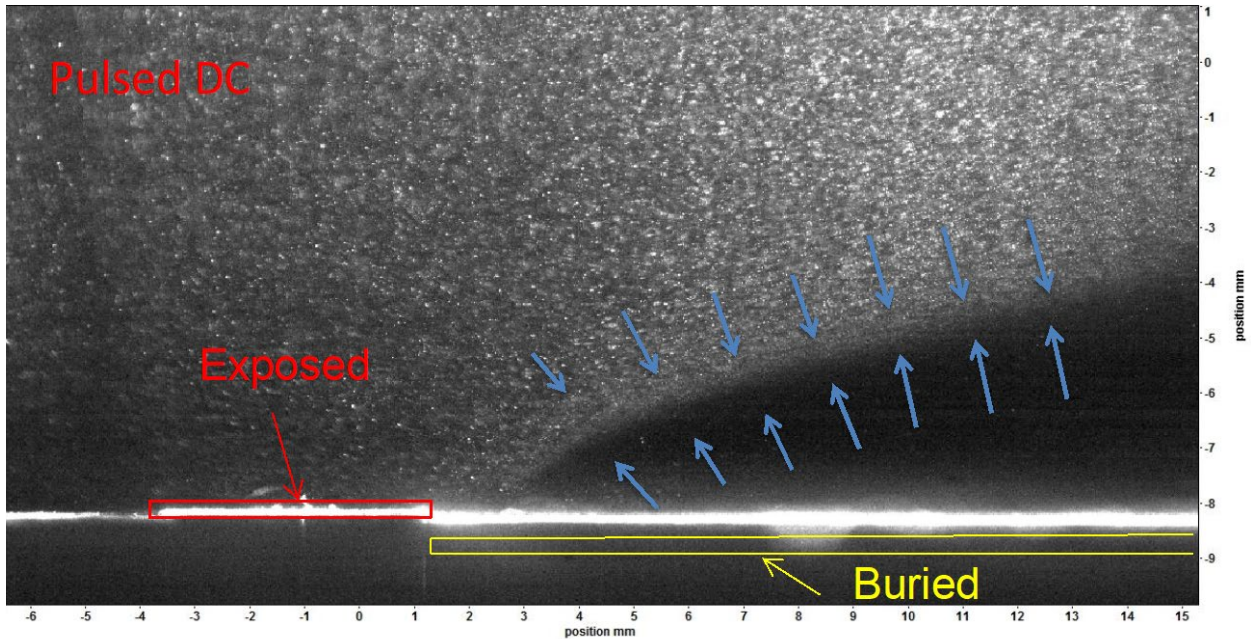**Figure 1. Sample drag reduction measurements obtained with a pulsed-DC plasma actuator array.**



**Figure 2. Particle separation in PIV measurements near the pulsed-DC actuator.**

American Institute of Aeronautics and Astronautics

Particle image velocimetry (PIV) was utilized in initial attempts to characterize the plasma-induced flow produced by the actuator in a quiescent environment (no external flow). Figure 2 presents a representative PIV image which shows an unusual region of particle separation emanating from the edge of the surface electrode and extending across the covered electrode. The measurements were performed in a large, closed test chamber that was uniformly seeded with 1-m Di-Ethyl-Hexyl-Sebacat (DEHS) particles. Of course, the particle separation prevented the determination of plasma induced flow velocity. The particle separation was found to be due to a dielectrophoretic force which transports the DEHS particles toward regions of high electric field intensity gradient. The dielectrophorectic force is given by,

$$\vec{F}_{DEP} = 2\pi\varepsilon_1 R^3 \left( \frac{\varepsilon_2 - \varepsilon_1}{\varepsilon_2 + \varepsilon_1} \right) \nabla E_0^2$$

where R is the radius of the DEHS particles, $\varepsilon_1$ is the permittivity of the medium (air =1) and $\varepsilon_2$ is the permittivity of the DEHS seed particles ($\varepsilon_2$=3.89) and $E_0$ is the electric field. The dielectrophoretic force arises because of the highly non-uniform electric field associated with operation of the pulsed-DC actuator.

The inability to use conventional PIV in order to characterize the plasma-induced flow produced by the actuator motivated the use of the optical methods that form the focus of this paper. Specifically, wavefronts were collected in the spanwise direction and analyzed to provide additional insight into the flow field over the plasma actuator. A similar approach was successfully used to measure mean velocity profiles in the wall-normal direction in a canonical subsonic BL [4], as well as wall-normal velocity and density profiles in a moderately heated or cooled subsonic BL [6]. The non-intrusive nature of the used optical method allows one to study the density and the velocity fields without placing any physical sensors in the region of very large unsteady electric fields. Results will be compared to the hot-wire measurements taken downstream of the plasma actuator. This comparison helps in interpreting optical results, with the goal of using the optical method to continue studying the BL properties immediately over the plasma actuator.

## II.    Pulsed-DC plasma actuator

Dielectric barrier discharge (DBD) plasma actuators have been of interest in areas of flow control for the past few decades. The advantages of such a flow control device are, but not limited to, fast time responses, ease of application and no mechanical parts. At the University of Notre Dame a new power system for DBD actuators that utilize a pulsed-DC waveform was developed [1,2]. The plasma actuator arrangement is identical to most typical AC-DBD geometries with staggered electrodes that are separated by a dielectric insulator, as shown in Figure 3.

The key difference is that the pulsed-DC actuator utilizes a DC voltage source to drive the actuator instead of an AC voltage input. This pulsed-DC actuator can be thought of as a hybrid system between a pure DC discharge and AC-DBD operation. The DC source is supplied to both electrodes. The exposed electrode remains constant in time while the encapsulated electrode is periodically grounded for short instances by way of a fast-acting solid state switch and is then allowed to rise back to the source DC level as shown in Figure 3. An input trigger signal determines the frequency at which the encapsulated electrode is grounded and the extent of time at which the electrode stays grounded. Ionization (plasma formation) occurs at each time in which the encapsulated electrode is grounded due to large charge build-up of electrons on the surface of the dielectric. The negative ions produced during this time are accelerated from the electric field,

following the electric field lines, colliding with other molecules. This results in a body force produced by the plasma field which produces the induced flow shown in Figure 2.
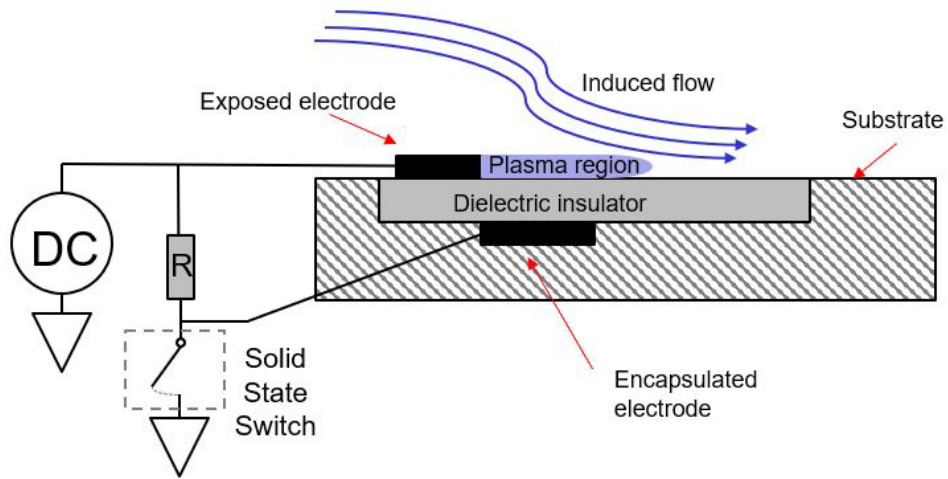


**Figure 3. Typical DBD plasma actuator geometry. Reproduced from [2].**

The actuator was fabricated using copper tape that was 0.004 inches thick for the two electrodes and with Ultem as the dielectric insulator which was 0.005 inches in thickness. The input trigger signal was a narrow pulse at a fixed pulse-width of 20μs at 500 Hz and 2 kHz forcing frequency shown in Figure 4.
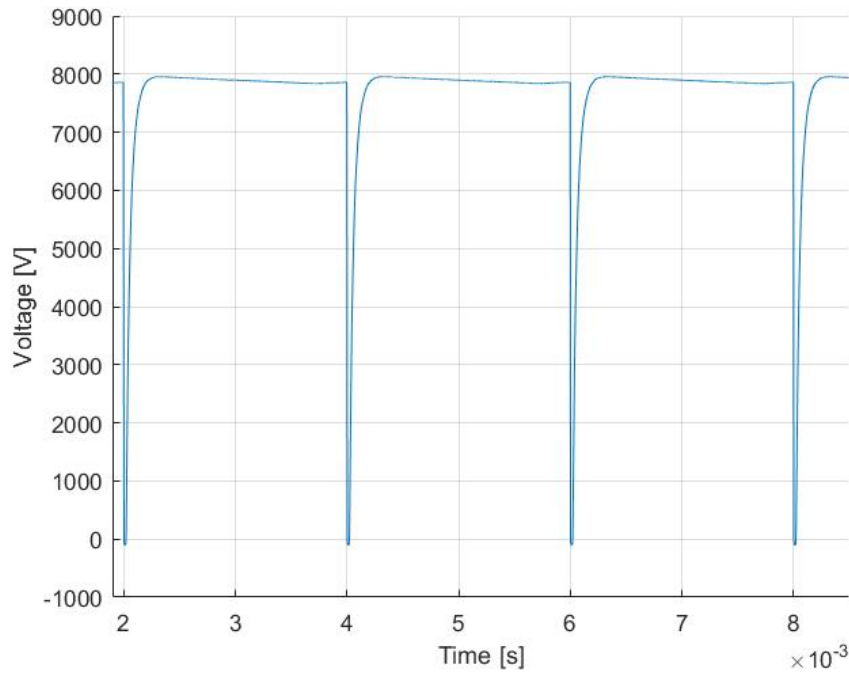


**Figure 4. Voltage time-series of encapsulated electrode.**

## III.    Experimental Setup

As plasma deposits the energy into the air and heats it up, the temperature variations will create density fluctuations near the plasma actuator. These density fluctuations essentially introduce

American Institute of Aeronautics and Astronautics

passive optically-aberrating markers into the flow, and they can be used to measure the velocity field near the actuator [7]. However, for the pulsed-DC plasma, see Figure 4, the plasma exists for a fraction of a millisecond, compared to a more conventional AC plasma, where it exists for most of the time. As a consequence, the amount of deposited thermal energy is small for the pulsed-DC setup and localized to the exposed electrode leaving any downstream fluid unheated. In addition, the Hessert Laboratory Atmospheric Wind Tunnel used in this study is a low speed tunnel with a cross sectional area of 1.5 m x 1.5 m, a test section length of 15.25 m, and a free stream velocity up to 13.5 m/sec.

For the presented turbulent boundary layer experiments, the tunnel freestream speed was 5.9 m/sec. At the measurement location, the boundary layer had a thickness of $\delta = 170$ mm, $\delta^+ = 3500$, and $Re_\tau = 3250$. For more details about the boundary layer statistics, see [12].

The flow regime at the tunnel's speeds is naturally incompressible and therefore requires thermal stimulus in order to become optically visible [8,9,10]. If the wall heating is moderate, it does not introduce any significant buoyancy effects, but simply "tags" the turbulent flow with slightly different temperature, or, equivalently density, regions. These slightly varying density regions can be measured using the optical method. To introduce temperature mismatch in the current experiments, a 12" x 12" heating pad was installed 1" upstream of the plasma actuator and heated to 110°F, using a proportional controller. Figure 5 shows the location of the heating pad upstream of the plasma actuator as well as the optical components in the test section and the measurement location at the trailing edge of the actuator.
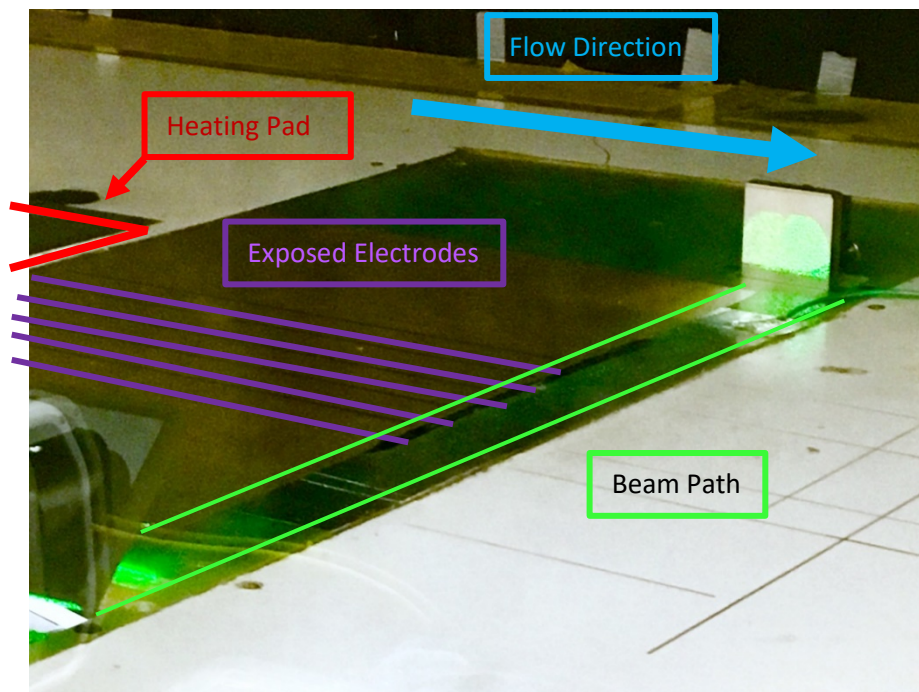


**Figure 5. Experimental setup of the Hessert Atmospheric Tunnel.**

In this study, the Shack-Hartmann wavefront sensor (WFS) was used to measure the actuator-related density fluctuations to study the flow over the pulsed-DC plasma actuator in both still air and for the turbulent boundary layer. The experimental set-up to quantify the flow generated by the actuator in still air is shown in Figure 6; a similar set-up is used to study the flow over the actuator in the turbulent boundary layer. The laser beam was expanded to a 2-in beam and

forwarded over a single plasma actuator in the direction perpendicular to the actuator electrode. After being reflected back by the return mirror along the same way it came and increasing the signal by a factor of two, the returned beam was split off and forwarded onto the high-speed camera, a Phantom v1610. The camera had a 38 mm focal length, with a 70 x 60 lenslet array attached, which splits the incoming beam into a rectangular array of smaller sub-aperture square beams and focuses each of them onto the sensor. Knowing the instantaneous dot position and the focal length of the lenslet array, the temporal deflection angle of each sub-aperture at different wall-normal and streamwise locations, $\theta(x,y,t)$, can be reconstructed. For the still air test, data were collected by the camera at a sampling frequency of 50 and 100 kHz with spatial resolutions varying from 512x320 down to 128x128 pixels with and without the lenslet array. Removing the lenslet array allowed for collecting shadowgraph data sets. In the case of the turbulent boundary layer, data was collected at 10, 5, and 2 kHz with a 384x288 pixels. It corresponds to the measured region of 25 mm x 20 mm, with the beam sub-aperture size in both wall-normal and the streamwise direction of 0.8 mm or $\Delta y^+ = 16.5$. A sample image with the wall location added is shown in Figure 7.
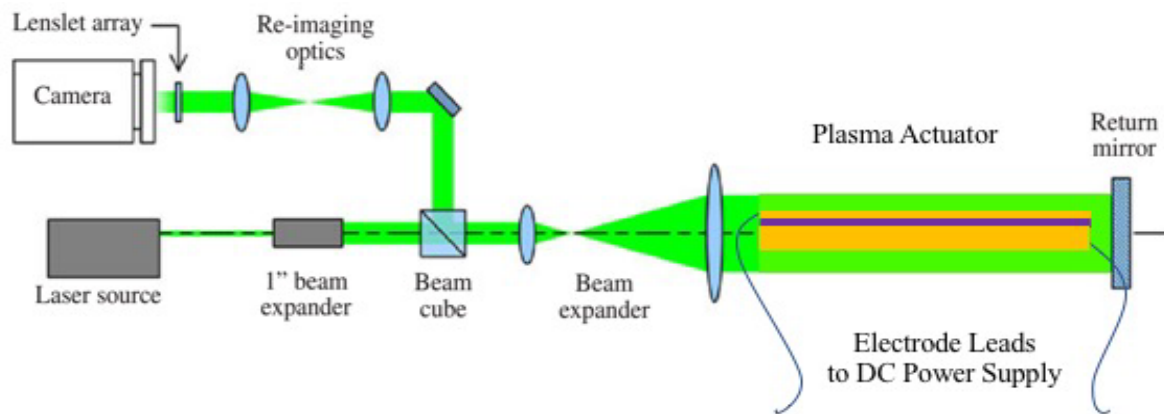


**Figure 6. Schematic of the Shack-Hartmann wavefront sensor and plasma actuator in the still air experiment.**
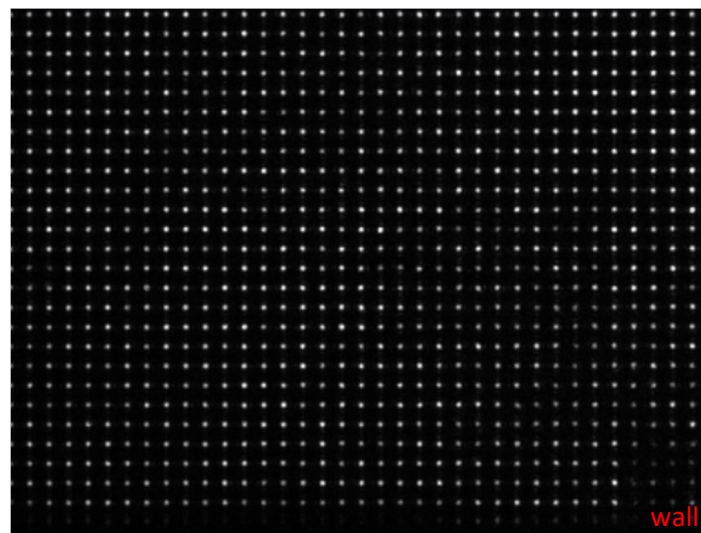


**Figure 7. Shack-Hartmann wavefront sensor image showing the location of the wall in the turbulent boundary layer experiment.**

For the still air case, the actuator was forced at 2 kHz at a voltage of 5 kV. In order to introduce a passive temperature mismatch, a block of dry ice was placed next to the actuator. As the ice sublimated, a layer of cool air developed over the exposed electrode. This cooled fluid lowered the baseline optical distortions to accentuate any temperature related distortions from the plasma.

For the turbulent boundary layer case, an array of plasma actuators was used. The electrodes were aligned in the streamwise direction; this arrangement was found to provide the largest decrease in the drag [2]. The electrode spacing was 1" with 5 electrodes and the overall size of the plasma actuator was 9" x 4".

From the measured deflection angles, the spectra of the streamwise component of the deflection angles, $\hat{\theta}(f)$, were computed for each lenslet sub-aperture. A critical assumption is made in calculating the convective velocity from $\hat{\theta}(f)$ spectra, namely the frozen flow assumption. This assumption allows the deflection angle spectra between two parallel beams, separated by a small distance, $\Delta$, in the flow direction, to be correlated and a convective time delay, $\tau$, between two signals to be calculated. Thus, the convective velocity can be experimentally calculated from the argument or the phase of the spectral cross correlation, $S(f) = \left\langle \hat{\vartheta}_1(f)\hat{\vartheta}_2^*(f) \right\rangle$, [4], where $\hat{\vartheta}_1(f)$ and $\hat{\vartheta}_2(f)$ denote the Fourier transforms of the time series of deflection angle from the upstream and downstream beams, respectively, and the star denotes the complex conjugate. Knowing the phase slope, the convective speed can be robustly calculated as $U_c = \Delta/\tau$, where the time delay $\tau$ is computed from the slope of the argument, $dArg[S(f)]/df = 2\pi\tau$.

Due to the nature of each sub-aperture producing a single signal, the physical size of each sub-aperture in effect sets the lower limit of the flow scales that are resolvable. Therefore, each sub-aperture should be sized based on the flow of interest.

In an effort to accurately measure the wall normal distance of the first row of sub-aperture beams, the lenslet array was removed before each trial and a sample image was recorded. This allows for the wall position on the image to be determined to within a few pixels.

For the still air test, in addition to the wavefront data, time-resolved shadowgraph images over the actuator in the spanwise direction were collected using the same experimental set-up by simply removing the lenslet array and repositioning the camera to make it more sensitive to the density variations caused by plasma.

## IV.   Results

Time-resolved shadowgraphs were processed to remove the time-averaged background image and analyzed. From Figure 4 it can be seen that when the voltage drops to zero, the plasma is formed during very short period of time and is present for a fraction of a millisecond. Analysis of the shadowgraph images during this period had revealed that the sudden air heating of plasma creates a weak compression wave, propagating outward from the actuator, see several successive images in Figure 8. This effect was also observed for nano-second plasma discharges [5].

Plasma introduces a body force, causing the flow to move away from the plasma region, and the heated flow region continues moving along the wall. Using optical diagnostics, this motion was observed in time-resolved phase-locked shadowgraphs. Figure 9 shows the image intensity variation along a horizontal line very close to the wall as a function of the horizontal distance and time, the so-called x-t plot. The plasma region can be seen as a highly optically disturbed region between x = 18 and 20 mm. the heated pockets of air moving away from the actuator can be seen

as diagonal bands between x = 20 and 25 mm. The slope of the band is related to the convective speed of the flow. Using the image in Figure 7, the convective speed was found to be 0.96 m/sec.
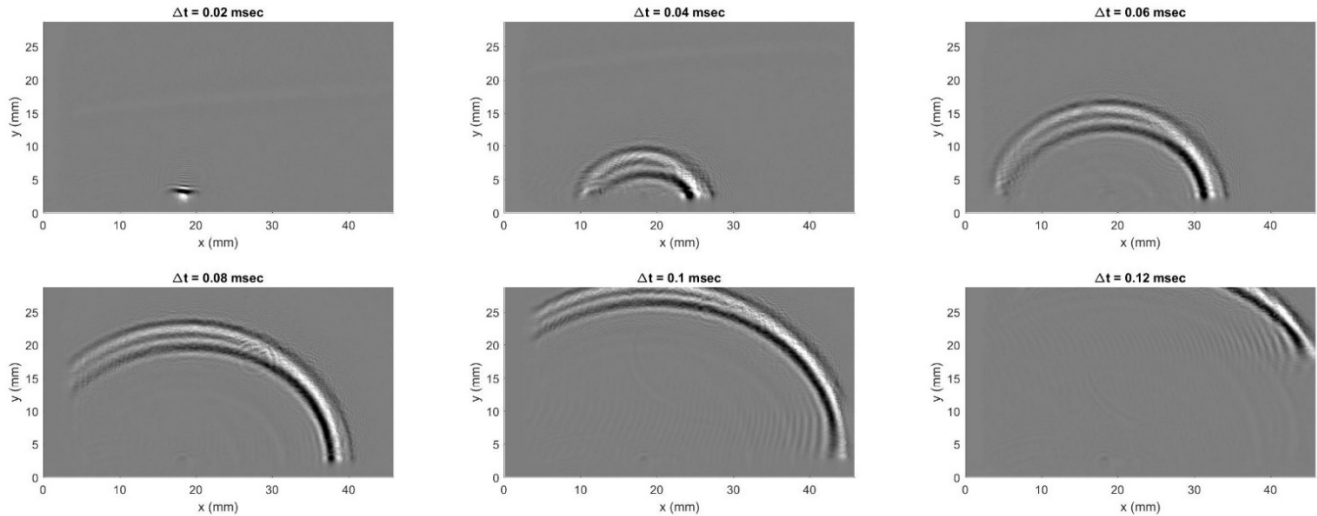


**Figure 8. Consecutive shadowgraph images, at and after the plasma is formed by the actuator, showing a compression wave created by the sudden thermal expansion. Image sampling frequency is 50 kHz.**
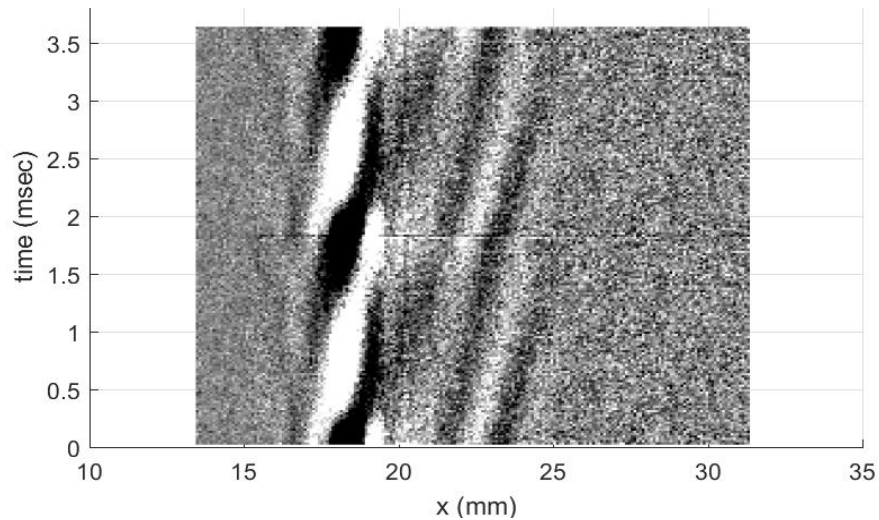


**Figure 9. Spatial-temporal evolution of the shadowgraph intensity near the wall in the vicinity of the actuator.**

As mentioned before, by cross-correlating deflection angles between multiple points it is possible to extract the time-averaged velocity profile at various distances away from the wall. This approach was successfully demonstrated for transonic turbulent boundary layers (TBL) in the previous studies [4,6], where the Shack-Hartmann wavefront sensor has been used to measure the mean velocity profile inside the TBL. The convective velocity in a TBL accurately follows a hotwire measured velocity profile through the majority of the boundary layer [4,6]. Only very near

the wall where velocity gradients are strongest and in the external portion of the boundary layer do the two profiles diverge. The good agreement achieved with the optically-related convective velocity method demonstrated that optical techniques can be used to measure flow properties of spanwise-uniform flows. As this optical technique does not require any seeding particles, it allows accurately measuring the velocity profile near the plasma actuator and to quantify the flow changes introduced to the TBL by the plasma without any interfering effects due to dielectrophoretic forces as discussed in the Introduction.

The convective velocity profile measured in the atmospheric tunnel boundary layer is presented in Figure 10. Due to the large boundary layer thickness, only the first 12% of the boundary layer or up to $y^+ = 413$ is resolved. The convective velocity computed using adjacent sub-apertures follows the hotwire profile with good agreement despite some scatter. However, the same computation using sub-apertures that are more than one sub-aperture apart (double, triple, or quadruple spacing) results in an unrealistically fast profile (1.3 times faster than the free stream). The reason for the overprediction in the current study is unknown and under continued investigation. It is theorized that this particular convective velocity profile is highly sensitive to a combination of sub-aperture spacing and the frequency range over which the velocity is computed. With that being said, the plasma does not show any sign of influencing the convective velocity profile one way or another. This result is consistent with the findings in a separate experiment [2], who found that downstream of the plasma actuator, only the $u_{rms}$ profile showed any changes due to the plasma, see Figure 11.
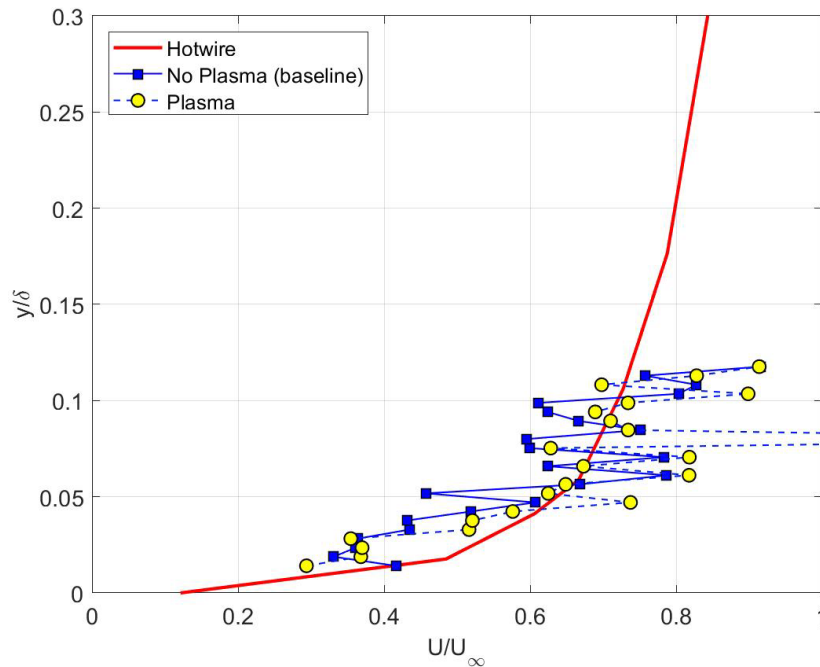


**Figure 10. Convective velocity profiles measured in the atmospheric tunnel. Hotwire profile provided courtesy of Samaresh Midya.**
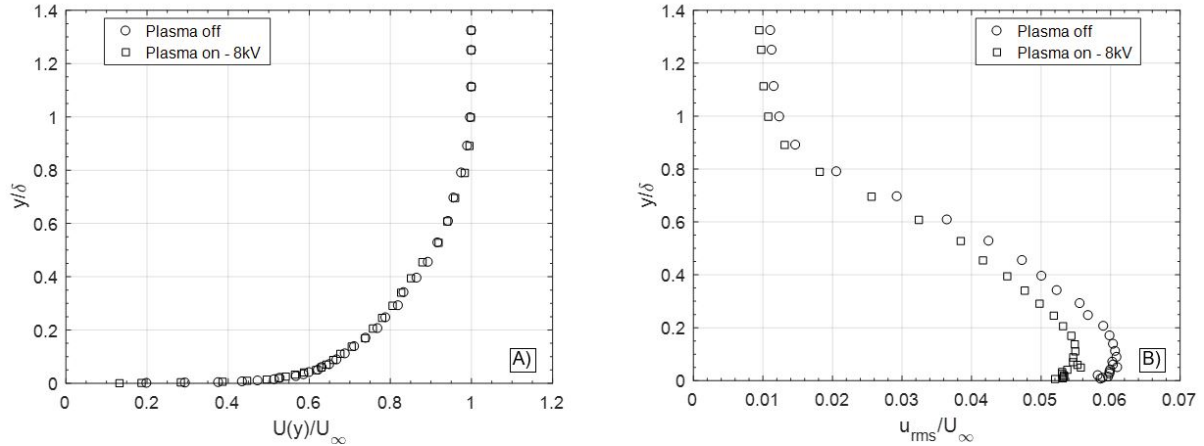
**Figure 11.** $\overline{U}$ **(left) and** $U_{rms}$ **(right) profiles measured in [2].**

Despite not seeing any discernable change in convective velocity profiles due to the plasma, deflection angle amplitude spectra may yield additional insight into the effect of the plasma. Using the spanwise uniform version of Sutton's linking equation [13] which links optical distortions, OPD, to density fluctuations,

$$OPD_{rms}^2(y) = 2K_{GD}^2 \rho_{rms}^2(y) \Lambda_z(y) L$$

combined with the Strong Reynold's Analogy and equation of state yields an equation for optical distortions in terms of constants and the mean and fluctuating velocity profiles,

$$OPD_{rms}(y) = K_{GD} \sqrt{2\Lambda_z(y)L} \frac{\rho_\infty M_\infty^2(\gamma - 1)}{\left[1 + \dfrac{\gamma - 1}{2} M_\infty^2\right]^2} \frac{\overline{U}(y)}{U_\infty} \frac{u_{rms}(y)}{U_\infty}.$$

This result shows that deflection angle spectra $\hat{\theta}$ should be proportional to $u_{rms}$.
With one last step linking deflection angle amplitude spectra to OPD,

$$OPD_{rms}^2 = 2U_c \int_0^\infty \frac{\left|\hat{\theta}(f)\right|^2}{(2\pi f)^2} df.$$

During the course of the experiment in the atmospheric tunnel, it was apparent that tunnel vibrations were inducing a global displacement in the camera image up to half of a sub-aperture. A method was developed by Smith et al. [11] to use the additional information contained in consecutive streamwise Shack-Hartmann sub-apertures to decompose the deflection angle amplitude spectra into stationary and convecting components. For a detailed description of this method, see [11]. Figure 12 shows an example of the spectral decomposition from the turbulent boundary layer experiment. The stationary component dominates in the low frequency range which is mostly associated with mechanical vibration of the tunnel and optical components. The convecting component only begins to dominate above 100 Hz and is primarily associated with aero-optical structures in the fluid flow. Not only is this method capable of filtering out signal contamination but it is also capable of making up for the lacking information in undersampled data. In Figure 12, in the highest frequency portion of the spectrum, the noise floor of the total signal is far higher in amplitude than either of the decomposed components.
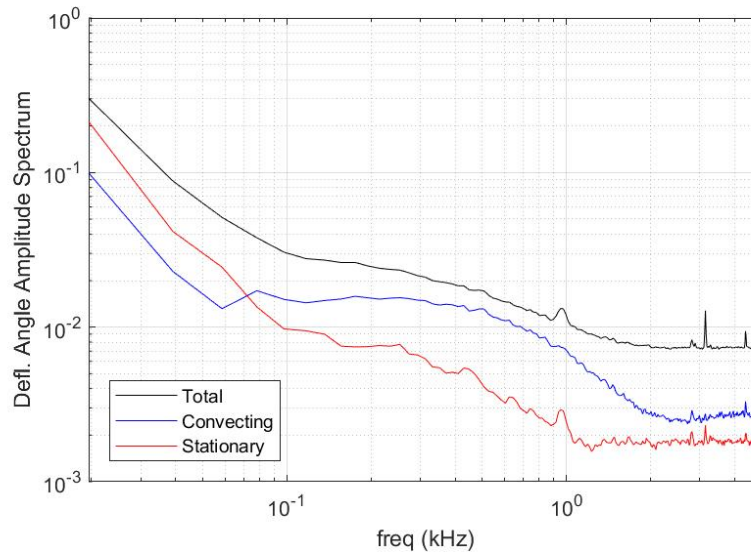
**Figure 12. Deflection angle spectrum decomposed into stationary and convecting components using multipoint analysis. y/δ = 0.05.**

In the turbulent boundary layer experiment, significant signal contamination is present due to tunnel vibration and therefore this method was used to isolate the convecting portion of the spectrum for further analysis. Figure 13 presents the convecting portion of the deflection angle spectrum for the first five wall normal points both with and without plasma present. The shape of the spectra are nearly identical between the two cases. The plasma itself was forced at 2 kHz but the spectra show no peaks at that frequency. This is most likely explained by the slow free stream velocity. From Figure 4, the plasma is generated for a short time every 2 msec, and the bulk velocity of the fluid flow transports the affected fluid less than a few millimeters before the next pulse. This results in a build up of plasma-affected fluid that has lost any information about the forcing that generated it.
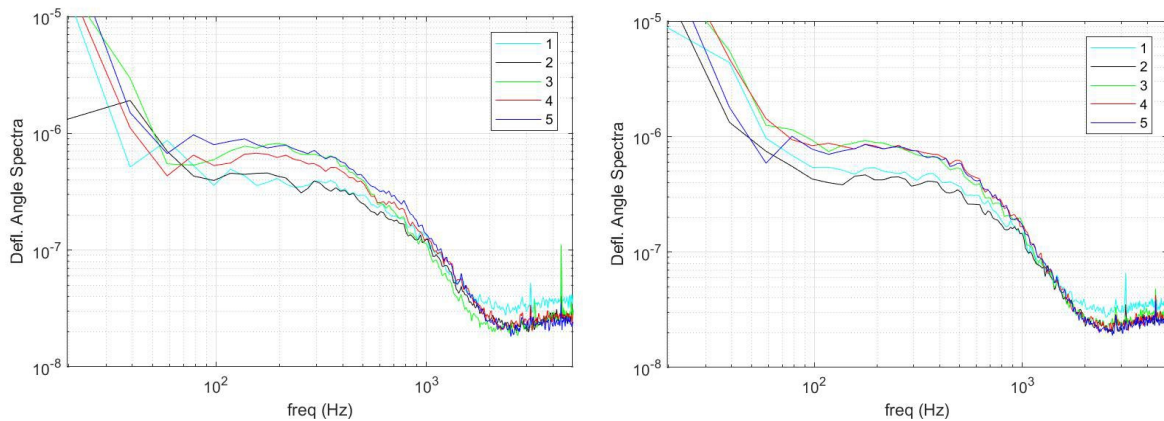


**Figure 13. Convecting portions of deflection angle spectra without (left) and with plasma (right) for the first 5 wall normal points.**

To get a better comparison between the plasma off and plasma on cases, the spectra at wall normal points of $y^+ = 16.5$, 33, 49.5, and 66 were plotted separately in Figure 14. The spectra for the plasma cases are consistently greater in amplitude than the no plasma baseline up to 1 kHz for

the first and fourth wall normal points. Above that, the plasma seems to have no effect on the spectra. This result indicates that at least for a measurement location at the trailing edge of the plasma actuator, the effect of the plasma is limited to the first few millimeters of the boundary layer. It is currently unknown why points two and three do not show significant change from the baseline. In general, the finding that the plasma spectra are increased in magnitude compared to the baseline is unexpected. As was shown in Figure 11, previous studies have shown that the plasma actuator dampens velocity fluctuations. Deflection angle amplitude spectra are proportional to velocity fluctuations so the plasma was expected to also decrease spectra. Further investigation needs to be made into the spectral decomposition as the spectra without decomposition showed the opposite trend.
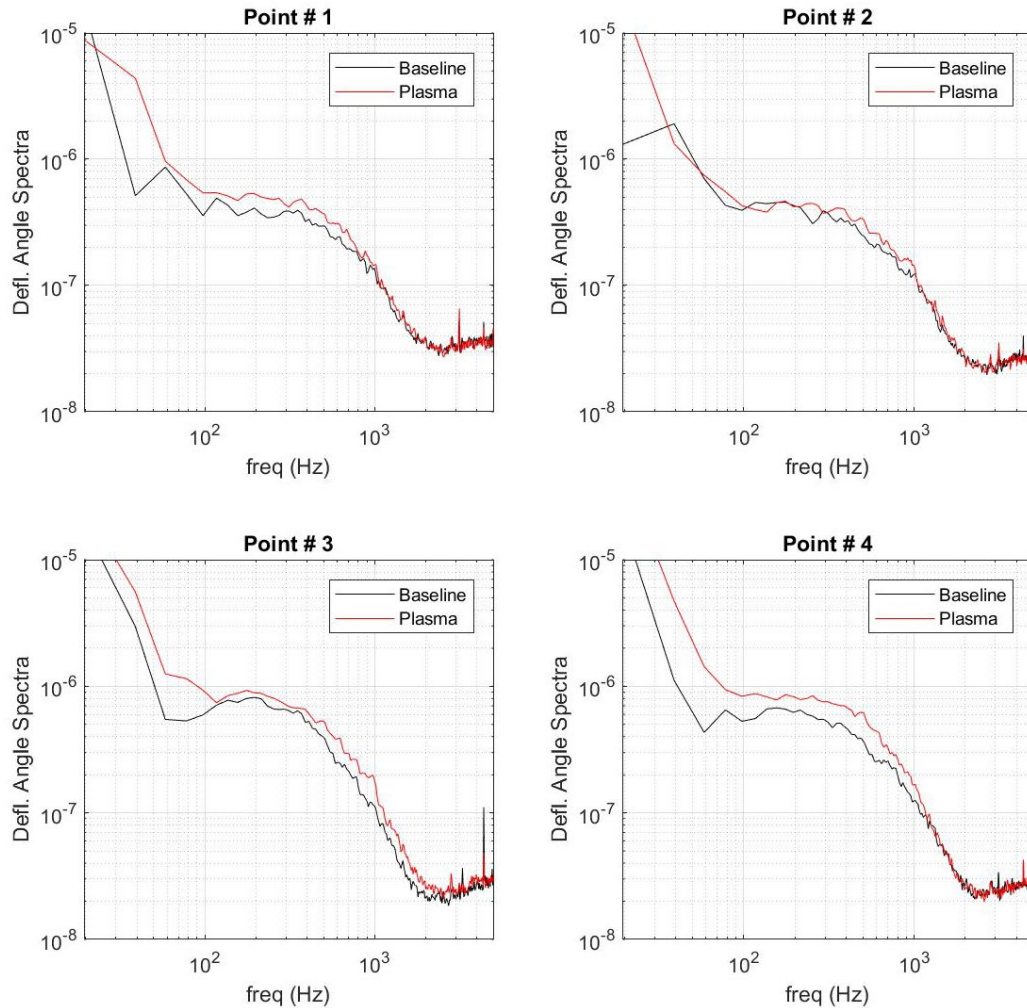
**Figure 14. Spectra comparison highlighting the influence of plasma at the wall normal locations closest to the wall.**

## V.    Conclusions

Several optical investigations into the nature of a pulsed-DC plasma actuator were conducted and presented. Shadowgraph measurements of the actuator in still air showed a weak compression wave being generated during plasma formation. In addition, an x-t plot of the shadowgraph images along the wall revealed an induced convective velocity of 0.96 m/s. However, with the introduction

of a free stream flow in the atmospheric tunnel, there was no discernable change in convective velocity due to the plasma.

A detailed spectral analysis was performed on the deflection angle data from the atmospheric tunnel test. Spectra were decomposed into stationary and convecting components in an effort to remove significant vibrational contamination. The convecting spectra was unchanged in form but increased in amplitude due to the plasma. This is in contradiction with past experiments that have shown that the plasma dampens velocity fluctuations which are proportional to amplitude spectra. No spectral spikes were seen at the plasma forcing frequency.

Overall, the presented optical measurements didn't reveal any significant changes in the boundary layer near the actuator. As the plasma actuator was demonstrated to significantly reduce the skin friction, neither the presented results nor the velocity studies downstream the plasma actuator showed any significant changes in the velocity field away from the actuator-affected wall. As there still many questions about the nature and the exact mechanism of the actuator-related drag reduction, additional experiments need to be conducted to fully understand the effect of the pulsed-DC plasma actuator. Data at additional measurement locations, both upstream and downstream of the trailing edge of the actuator, needs to be collected to understand the evolution and dissipation of the plasma effect.

## Acknowledgments

## References

[1] T. Corke, F. Thomas, A. Duong and R. McGowan, "Turbulent Boundary Layer Drag Reduction Through Plasma Streak Transient Growth Instability Control," AIAA SciTech 2017, 2017.

[2] A. Duong, T. Corke, F. Thomas, and K. Disser, " Turbulent Boundary Layer Drag Reduction via Pulsed-DC Plasma Actuation," submitted to J. Fluid Mech., 2018.

[3] W. Shoppa and F. Hussain, "Coherent structure generation on near-wall turbulence," J. Fluid Mech., Vol. 453, pp. 57-108, 2002.

[4] J. Sontag and S. Gordeyev, "Non-intrusive Velocity and Density Measurements in Subsonic Turbulent Boundary Layer," AIAA Paper 2015-3247, 2015.

[5] Leonov, S, Petrishchev, V and Adamovich, I "Dynamics of energy coupling and thermalization in barrier discharges over dielectric and weakly conducting surfaces on us to ms time scales," J. Phys. D: Appl. Phys., 47, 465201, 2014.

[6] J. Sontag and S. Gordeyev, "Studies of Density Fields in Non-Adiabatic Boundary Layers Using Wavefront Sensors", AIAA Paper 2017-3835, 2017.

[7] C. L. Enloe, T. McLaughlin, G.I. Font, and J.W. Baughn,"Parameterization of Temporal Structure in the Single-Dielectric-Barrier Aerodynamic Plasma Actuator", AIAA Journal, 44(6), pp. 1127-1136, 2006.

[8] A.E. Smith, S, Gordeyev, T. Saxton-Fox and B. McKeon, "Subsonic Boundary-Layer Wavefront Spectra for a Range of Reynolds Numbers," AIAA Paper 2014-2491, 2014.

[9] S. Gordeyev, A.E. Smith, T Saxton-Fox and B. McKeon, "Studies of the large-scale structure in adiabatic and moderately-wall-heated subsonic boundary layers," Paper 7A-3, 9th International Symposium on Turbulence and Shear Flow Phenomena (TSFP-9), 2015.

[10] T.Saxton-Fox, B.J. McKeon and S Gordeyev, "Effect of coherent structures on aero-optic distortion in a heated turbulent boundary layer," submitted to AIAA Journal, 2018.

[11] A.E. Smith, S. Gordeyev, H. Ahmed, A. Ahmed, D.J. Wittich III and M. Paul, "Shack-Hartmann Wavefront Measurements of Supersonic Turbulent Boundary Layers in the TGF," AIAA Paper 2014-2493, 2014.

[12] S. Midya, F. O. Thomas and T. C. Corke, "A Local Nonlinear System Model of the Turbulent Boundary Layer," Paper 7B-6, 10th International Symposium on Turbulence and Shear Flow Phenomena (TSFP-10), 2017.

[13] Sutton, G.W., "Effect of Turbulent Fluctuations in an Optically Active Fluid Medium," AIAA Journal 7(9), 1737-1743 (1969).